Maxwell: A Semi-analytic 4D Code for Earthquake Cycle Modeling of Transform Fault Systems

David Sandwell[a], Bridget Smith-Konter[b]

[a] *Scripps Institution of Oceanography*
[b] *University of Hawaii at Manoa*

Abstract

We have developed a semi-analytic approach (and computational code) for rapidly calculating 3D time-dependent deformation and stress caused by screw dislocations imbedded within an elastic layer overlying a Maxwell viscoelastic half-space. The *maxwell* model is developed in the Fourier domain to exploit the computational advantages of the convolution theorem, hence substantially reducing the computational burden associated with an arbitrarily complex distribution of force couples necessary for fault modeling. The new aspect of this development is the ability to model lateral variations in shear modulus. Ten benchmark examples are provided for testing and verification of the algorithms and code. One final example simulates interseismic deformation along the San Andreas Fault System where lateral variations in shear modulus are included to simulate lateral variations in lithospheric structure.

Citation: Sandwell, D., B. Smith-Konter, (2018), Maxwell: A Semi-analytic 4D Code for Earthquake Cycle Modeling of Transform Fault Systems, *Computers and Geosciences*, 10.1016/j.cageo.2018.01.009.

1. Introduction

The quasi-static part of the earthquake cycle spans time scales of days to thousands of years and length scales of kilometers to thousands of kilometers. A variety of numerical methods have been developed for modeling earthquake cycle processes. The simplest screw dislocation models consist of 2D or 3D dislocations in a uniform elastic half-space (e.g., Weertman [1964]; Okada [1985]). These analytic models are commonly used for simulation of co-seismic slip and afterslip, and because of their speed and simplicity, are suitable for slip inversions using geodetic data Simons et al. [2002]; Bürgmann et al. [2002]. More complex numerical models can include more realistic geometries and rheologies but usually they require significant computer time to simulate the diverse length and time scales needed to model even postseismic processes (e.g., Takeuchi and Fialko [2013]).

More recently, full 3D models with realistic rheologies have been developed using an iterative spectral approach (e.g., Barbot and Fialko [2010]). Nevertheless, these novel approaches require a significant amount of computer time and memory to simulate postseismic processes. Our objective is to develop the theory and computer code that can capture some essential characteristics of the earthquake cycle and is also fast enough to calculate high spatial density ($\sim$1 km) Green's functions for inversions using GPS and InSAR data. We contend that the most important characteristics missing from elastic half-space Okada-type models are an asthenosphere response (relaxation) and the restoring force of gravity. Moreover, there are two aspects of the earthquake cycle that can only be well-simulated using models with a plate-like (lithosphere and asthenosphere) structure. The first is that during the interseismic part of the cycle, a thin elastic plate can deform internally more readily than an elastic half-space Thatcher [1983]. For example, far from a transform fault system we expect that the fault parallel velocity will be steady with time, while close to the fault the motion will be episodic. An lithosphere-asthenosphere model with a thin elastic plate over a viscoelastic half-space enables the strain field to diffuse from near the fault to the far field in a physically plausible way, guided by the asthenosphere viscosity and rigidity Pollitz [1997]. Second, the restoring force of gravity on a thin elastic plate over a viscoelastic half-space enables large spatial scale butterfly patterns surrounding active faults with subsidence in the compressional quadrants following major strike-slip earthquakes Pollitz et al. [2001] and slow uplift in the compressional quadrants during the interseismic period Smith and Sandwell [2004]; Howell et al. [2016]. Propagator methods (e.g., Rundle and Jackson [1977]; Pollitz [1997]; Fukahata and Matsu'ura [2006]) can capture these thin-plate processes, although the speed and numerical stability of the computer codes make it difficult to develop inverse models of complicated fault systems over many earthquake cycles Chuang and Johnson [2011].

Over the past 15 years we have developed a semi-analytic model and code for rapidly calculating surface deformation and stress associated with dislocations in an elastic plate over a viscoelastic half-space. Speed and numerical stability are achieved by explicitly solving the differential equations in the vertical dimension so the numerical propagator approach is not needed. The initial step in the theory and coding of the elastic plate model was to develop the Green's functions for the response of an elastic half-space to a 2D vector body force. Following Steketee [1958], we Smith and Sandwell [2003] developed a fully elastic half-space model of interseismic deformation. The method of images was used to partially satisfy the surface zero traction boundary conditions. The remaining non-zero vertical traction was balanced by imposing a vertical load on the surface.

The innovative aspect of this approach was the numerical treatment of curved fault segments and the use of the convolution theorem to dramatically reduce the processing time for faults with thousands of segments. Curved fault dislocations were simulated as numerous small (~2–5 km length) straight force double-couples imbedded in two grids for the generation of x- and y-direction body forces (Figure 0). In our method, Green's functions were developed in the Fourier transform (FT) domain, where the basic approach was to FT each of the body force grids, multiply the transform by the appropriate displacement or stress FT Green's function, and inverse transform to obtain the desired results (surface displacement or stress at depth). This explicit use of the convolution theorem provided computation speeds that greatly exceeded even the simplest Okada-type models. For example, computation of co-seismic displacement along a 50 km length curved fault on a 512×512 km grid (1 km grid cell spacing) requires only one second of CPU time on a standard laptop computer. One limitation of this approach is that the fault segments must be vertical over some finite depth range ($d_1 \leftrightarrow d_2$ in Figure 0) since we performed this integration analytically. Also, new Green's functions must be computed when either d_1 or d_2 is changed along a curved fault.

This method was extended to simulate an elastic layer over a viscoelastic half-space Smith and Sandwell [2004]. The extension used an infinite set of body force source and sink images above and below the surface of the Earth to match the horizontal zero-traction surface boundary conditions, as well as the continuity of displacement and stress at the base of the elastic layer Rybicki [1971]; Rundle and Jackson [1977]. As in the elastic half-space development, the non-zero vertical surface traction was balanced by a vertical force applied to an elastic plate over

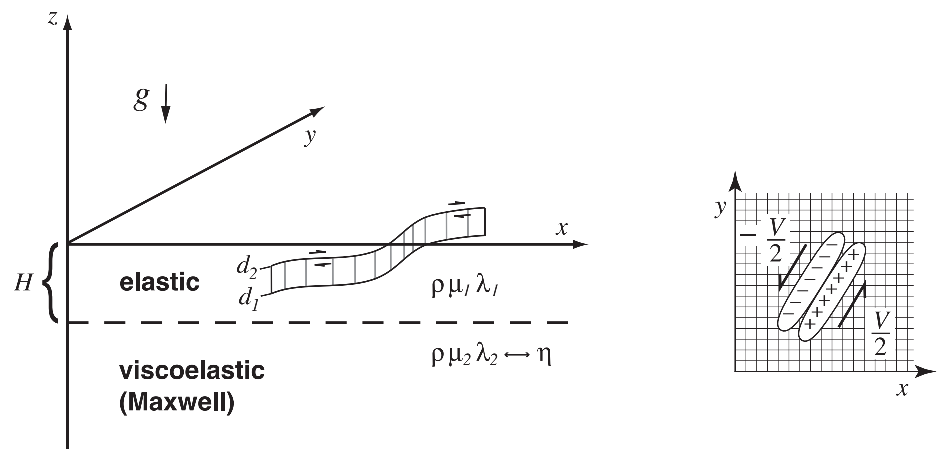

Figure 0: Schematic of the model simulating an elastic layer of thickness H overlying a linear maxwell viscoelastic half-space of viscosity η. (left) Fault elements extend from a lower depth of d_1 to an upper depth of d_2. A displacement discontinuity across each fault element is simulated using a finite width force couple as described in Smith and Sandwell [2004]. (right) There are two grids of force couples for the x and y components. The solution is fully analytic in the z direction so no gridding is needed. As described below, the upper layer has elastic constants that can vary laterally but not vertically. The elastic constants in the half-space are adjusted using the viscoelastic correspondence principle as described in Smith and Sandwell [2004].

a half-space of differing rigidity. Similarly, the unbalanced vertical traction at the base of the elastic layer was balanced by a vertical force applied at depth. The rigidity of the underlying half-space was varied using the correspondence principle to simulate a viscoelastic response Nur and Mavko [1974]. This approach has been used to construct 4D models of displacement and stress of the San Andreas Fault System spanning the past 1000 years that are able to match the present-day geodetic data (GPS and InSAR) as well as geologic slip rates Smith and Sandwell [2006]; Smith-Konter and Sandwell [2009]; Tong et al. [2014].

Here we add an additional 2D spatial variation in body forces to simulate 2D spatial variations in elastic constants $[\lambda(\vec{x}), \mu(\vec{x})]$. The basic approach is to decompose the elastic constants into a mean value and a 2D spatially variable part (e.g., Barbot et al. [2008, 2009]; Segall [2010]). The mean value is used for computation of the Green's functions as in Smith and Sandwell [2004]. We use the method of successive approximations to solve for the 2D spatial variations in body forces that will be added to the dislocation body forces to provide the solution. This approach was used for variable rigidity flexure studies Sandwell [1984]; Garcia et al. [2014] as well as 2D and 3D elasticity problems Barbot et al. [2008, 2009]. Those studies provided formal convergence criterion based on the properties of the Green's function and the smoothness of the spatial variations in flexural rigidity. The Green's functions used in this study are too complex to develop a formal convergence criterion so we explore the convergence numerically by varying the strength and roughness of the rigidity variations.

After presenting the variability rigidity method, we introduce and describe the freely-available software used for earthquake cycle modeling (*maxwell.f*). The code is tested using 10 benchmark cases, as well as a full 3D example of the San Andreas Fault System (SAFS). Appendix A and an open source GitHub distribution provide all of the scripts to reproduce the benchmark examples. Since the modeling is performed in a 3D Cartesian coordinate system, all of the data and model geometry must be re-projected from latitude and longitude into a Cartesian space where the y-axis lies along a small circle of the best pole of rotation (i.e., Wdowinski et al. [2007]) of the transformed (Cartesian) fault system. The code and documentation for performing this transformation on scalar, vector, and tensor quantities is provided in Appendix B.

2. Method

To provide an overview of the successive approximation method we follow the notation of Barbot et al. [2008]. We begin with the usual equations relating 3D displacement to strain as

$$\varepsilon_{ij} = \frac{1}{2}\left(u_{i,j} + u_{j,i}\right) \tag{1}$$

where u_i is the 3D displacement vector and ε_{ij} is the strain tensor. Then we relate stress to strain

$$\sigma_{ij} = \lambda\left(\vec{x}\right)\delta_{ij}\varepsilon_{kk} + 2\mu\left(\vec{x}\right)\varepsilon_{ij} \quad \text{or} \quad \underset{\sim}{\sigma} = \underset{\sim}{C} : \underset{\sim}{\varepsilon} \tag{2}$$

where λ and μ are the Lame parameters that vary spatially in the two horizontal dimensions $\vec{x} = (x, y)$. The Lame parameter $\lambda\left(\vec{x}\right)$ is related to the shear modulus by a spatially uniform Poisson's ratio. $\underset{\sim}{C}$ is the elastic moduli tensor (underscore denotes a tensor throughout) and the operation ':' refers to the double scalar product. The quasi-static equilibrium equations are

$$\nabla \bullet \underset{\sim}{\sigma} + \vec{\rho} = 0 \quad \text{or} \quad \nabla \bullet \left(\underset{\sim}{C} : \underset{\sim}{\varepsilon}\right) + \vec{\rho} = 0 \tag{3}$$

where $\vec{\rho}$ is the vector body force. As in the previous publications, we decompose the elastic parameters into a constant and variable part.

$$\lambda\left(\vec{x}\right) = \lambda^0 + \lambda'\left(\vec{x}\right) \quad \mu\left(\vec{x}\right) = \mu^0 + \mu'\left(\vec{x}\right) \tag{4}$$

We can rewrite the elasticity tensor in a similar notation

$$\underset{\sim}{C}\left(\vec{x}\right) = \underset{\sim}{C}^0 + \underset{\sim}{C}'\left(\vec{x}\right) \tag{5}$$

Plugging this into the equilibrium equation we arrive at

$$\nabla \bullet \left(\underset{\sim}{C}^0 : \underset{\sim}{\varepsilon}\right) + \nabla \bullet \left(\underset{\sim}{C}' : \underset{\sim}{\varepsilon}\right) + \vec{\rho} = 0 \tag{6}$$

We can rewrite this expression as

$$\nabla \bullet \left(\underset{\sim}{C}^0 : \underset{\sim}{\varepsilon}\right) = -\left[\vec{\rho} + \nabla \bullet \left(\underset{\sim}{C}' : \underset{\sim}{\varepsilon}\right)\right] \tag{7}$$

Note that the second term on the right side is an additional component of body force to be added to the initial body force to satisfy the equilibrium equation.

We solve this problem by successive approximation. First we use the Green's function to solve the problem for the case of horizontally uniform elasticity. We can write this in a formal way in the FT domain as

$$\vec{u}\left(\vec{k}, z\right) = \underset{\sim}{\Omega}^u\left(\vec{k}, z\right)\vec{\rho}\left(\vec{k}\right) \tag{8}$$

where $\vec{k} = \left(k_x, k_y\right)$ is the 2-dimensional wavenumber, z is the observation depth, and $\underset{\sim}{\Omega}^u$ is a tensor function to map a 2D distribution of horizontal vector body forces into a 3D displacement (or strain). There is a similar expression for mapping the body forces into a strain tensor.

$$\underset{\sim}{\varepsilon}\left(\vec{k}, z\right) = \underset{\sim}{\Omega}^{\varepsilon}\left(\vec{k}, z\right)\vec{\rho}\left(\vec{k}\right) \tag{9}$$

We begin the iteration by first solving the problem for the uniform elasticity resulting in an initial estimate of the strain tensor $\underset{\sim}{\varepsilon}^0$. We then insert this initial estimate of the strain tensor into the right hand side of equation (7) and rewrite the body force as

$$\vec{\rho}^{\,1} = \vec{\rho}^{\,0} + \nabla \bullet \left(\underset{\sim}{C}' : \underset{\sim}{\varepsilon}^0\right) \tag{10}$$

Note that while the strain tensor has spatial variations in 3-dimensions, the vertical derivatives of $\underset{\sim}{C}$ are zero. Here we make an approximation that the vertical variations in strain are small so we can use strain calculated at a single depth as a proxy for the strain averaged between the depths where the original body force was applied. Under this assumption, the updated body force vector remains a 2D vector. Below we will discuss the optimal depth for calculating this 2D strain. The basic iteration is straightforward. One introduces the usual 2D vector body force array and solves for the displacement and strain fields using equations (8, 9). This is already implemented in the standard *maxwell* code. Given this initial estimate of the strain field one calculates new grids of the 2D vector body force using equation (10). The updated grids of vector body force are inserted into (9) to provide an updated estimate of the strain field and the steps are repeated until convergence is reached. This treatment of variable rigidity is now implemented in the *maxwell* code.

In practice, the strain update (9) is best done by multiplication in the FT domain while the tensor product $\underset{\sim}{C} : \underset{\sim}{\varepsilon}^0$ is best done by multiplication in the space domain so no convolutions are needed. Therefore, each iteration requires 6 (2D) FT operations. We use single precision arrays for storage and double precision for some numerical calculations, so the *maxwell* program allocates about 1 GB of memory for the full SAFS example (4096 × 4096 grid cells). The computer time for this example (next described in BM11) is 134 seconds on a MacBook Pro with a 3 GHz processor. We use the GMT library for reading and writing netcdf files from FORTRAN, but this could be easily replaced with generic I/O routines.

As discussed in the introduction, one can make a formal proof of convergence for the 2D variable flexural rigidity case Garcia et al. [2014] as well as the 1D variable elasticity case Barbot et al. [2008]. In both cases, convergence requires that the convolution of the source spectra with the variable elasticity spectra does not have any power at the Nyquist wavenumber of the grid being used for the calculation. For example, convergence is guaranteed if the source and elasticity spectra both have zero power at 1/2 the Nyquist wavenumber.

One question that arises is what is the optimal depth to compute the strain to perform the update of the body force. We calculated the strain at 3 depths to determine which depth provided the best match to the benchmark solutions. These depths are: (1) the surface of the Earth, (2) half way between the surface and the top of the fault, and (3) the top of the fault. For simple cases (e.g. BM2-4 below) the two shallower depths provide similar results. The deeper depth sometimes provided anomalous results because of the strain singularity at the top of the fault. For the most challenging case (BM3 below), we found that the strain calculated half way between the surface and the top of the fault provided a best match to the analytic solution. The misfit for these 3 locations for BM3-4 is discussed below.

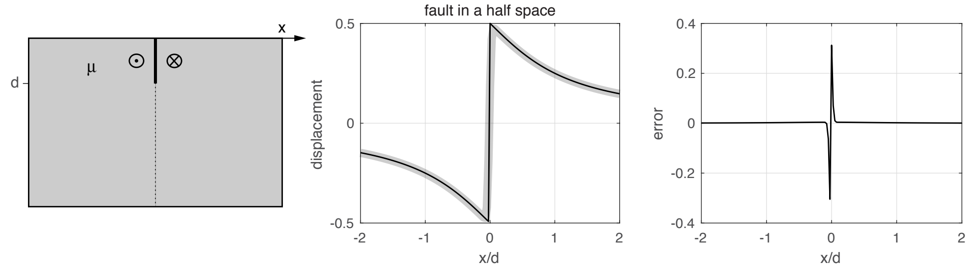

Figure 1: (left) Strike-slip fault in an elastic half-space where slip is uniform to a depth d. (center) The semi-analytic *maxwell* calculation of fault-perpendicular surface displacement (grey line) is compared with the analytical solution (black line). Both solutions have zero displacement for large x/d. (right) The largest differences occur above the force couple, which has a finite width, and so cannot simulate a perfect step. The standard deviation of the differences is 0.022 or about 4% of the maximum amplitude.

3. Benchmarks

Ten displacement benchmark (BM) comparisons are used to verify the numerical accuracy of the *maxwell* computer code. The first 8 benchmarks are comparisons with analytic solutions. Most are provided in the book on *Earthquake and Volcano Deformation* Segall [2010]. The last two are test cases using propagator software Fukahata and Matsu'ura [2006] (*K. Johnson*, personal communication). For all 2D benchmark cases (BM1–7), we initialized the *maxwell* code with body force arrays having dimensions of 16 cells in the fault parallel direction (this could have been dimensioned as 2, given the zero contribution of the fault parallel component for an infinitely long fault plane) and 8192 cells in the fault-perpendicular direction. For the 3D examples (BM8–11), we initialized the force arrays to 4096 by 4096 cells. The *maxwell_v* code requires 14 of these arrays.

BM1. Model of a 2D screw dislocation with unit slip extending from the surface to a depth d in a uniform elastic half-space (Figure 1). The analytic solution is derived in Weertman [1964] and provided as equation 2.26 in Segall [2010] where we set $d_1 = d$ and $d_2 = 0$. In this case of uniform rigidity μ, the strength of the force couple needed to produce slip s is $\rho = \mu s$ Burridge and Knopoff [1964]. Below we will see that for non-uniform rigidity, there is not always a simple relationship between slip and force.

BM2. Model of a 2D screw dislocation extending from the surface to a depth d in an elastic plate overlying a fluid half-space (Figure 2). The analytic solution is derived in Rybicki [1971] and provided as equation 5.33 in Segall [2010]. Note that the displacement far from the fault does not go to zero as in the half-space example (Figure 1) and in this case the far-field displacement is 1/2 the maximum displacement because the fault cuts half way through the elastic layer. As in BM1 we have used the relationship $\rho = \mu s$.

BM3. Model of a 2D screw dislocation extending from a depth d to infinite depth in an elastic medium with a sharp rigidity contrast (Figure 3). The analytic solution is derived in Segall [2010], equation 5.11. As discussed in the *Methods* section above, this lateral variation requires

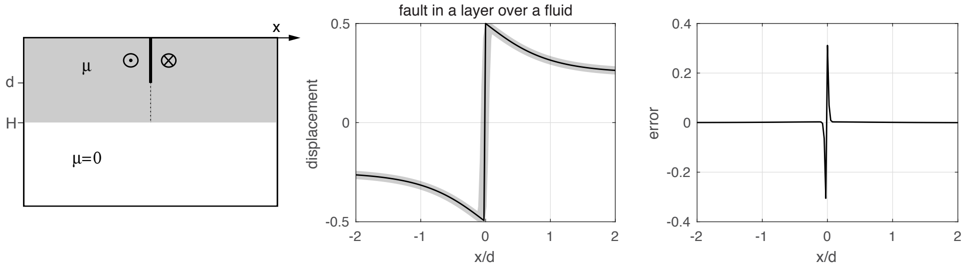

Figure 2: (left) Strike-slip fault in an elastic plate of thickness H over a fluid half-space where slip is uniform to a depth d. (center) The semi-analytic *maxwell* calculation of fault-perpendicular surface displacement (grey line) is compared with the analytical solution (black line). Both solutions have a displacement of 0.25 at large x/d. (right) As in Figure 1, the largest differences occur above the finite-width force couple. The standard deviation of the differences is 0.022 or about 4% of the maximum amplitude.

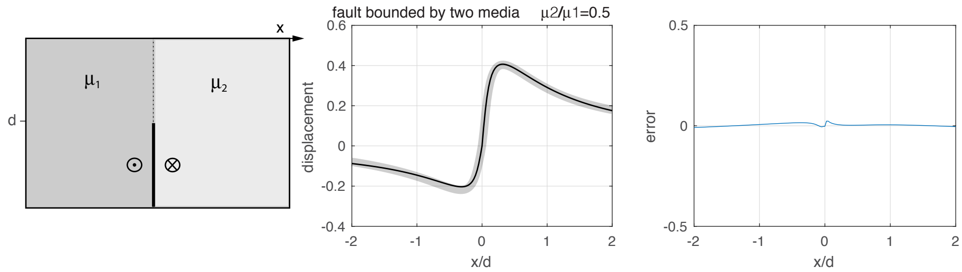

Figure 3: (left) Strike-slip fault bounding two media that has uniform slip from depth d to infinite depth. (center) The numerical *maxwell_v* calculation of the surface displacement (grey line) is compared with the analytical solution (black line). (right) The largest differences occur above the force couple. The standard deviation for the 3 depths of strain calculation (surface, half to top of fault, and top of fault) are 0.0134, 0.0132, and 0.0171, respectively. The best case is 3.3% of the maximum amplitude.

iteration to update the body forces. Convergence is reached after 10 iterations when the maximum difference from the final solution (e.g. 20 iterations) is less than 10^{-6}. The 2D strain tensor was calculated at a depth of $d/2$. This selection of depth provides the closest match to the analytic result. We note that this benchmark was the most challenging of all 10 benchmarks because the step in rigidity and the body force couple occur at the same location. Achieving convergence required that the rigidity step be low-pass filtered at a wavelength of 4 times the grid spacing. In this case, the strength of the body force is related to the average rigidity of the model $\rho = s(\mu_1 + \mu_2)$.

BM4. Model of a 2D screw dislocation extending from a depth d to infinite depth in an elastic medium with a compliant zone (Figure 4). The analytic solution for unit slip is derived in Segall [2010], equation 5.23. This variable rigidity example also required 10 iterations to converge. As in BM3, the strain used for the iteration update was computed at a depth of $d/2$. Note that the *maxwell* code uses a force couple with strength $\mu_1 s$. Because the compliant fault zone has a lower rigidity than the surrounding material, the amplitude of the displacement is larger

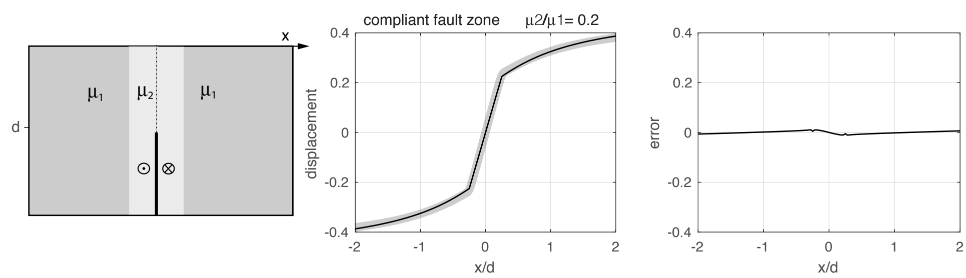

Figure 4: (left) Strike-slip fault within a compliant zone with uniform slip from depth *d* to infinite depth. (center) The numerical *maxwell_v* calculation of the surface displacement (grey line) is compared with the analytical solution (black line). The numerical solution was scaled by a factor of 0.53 to best match the analytic solution. (right) The largest differences occur at the boundaries of the compliant zone. The standard deviation for the 3 depths of strain calculation (surface, half to top of fault, and top of fault) are 0.011, 0.012, and 0.313, respectively. The best case is 2.7% of the maximum amplitude.

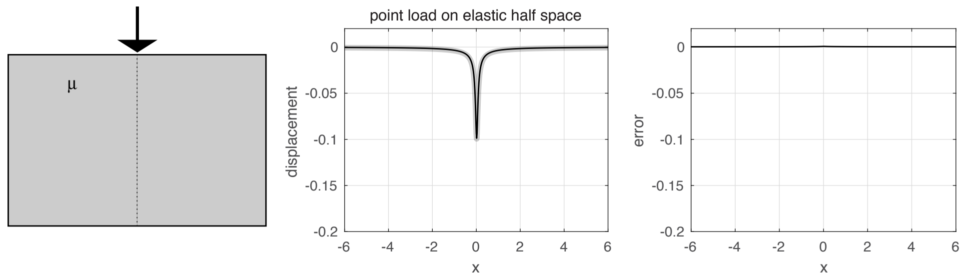

Figure 5: (left) Point load on an elastic half-space. (center) The semi-analytic *maxwell* calculation of the surface vertical displacement computed at a depth of 4 times the horizontal grid cell spacing (grey line) is compared with the analytical solution computed at the same depth (black line). The differences are very small. The standard deviation of the difference is 0.0001 which is about .1% of the maximum amplitude.

for the *maxwell* solution than for the analytic solution. Unlike cases 1-3, there is no simple relationship between the strength of the force couple and the slip; a scale factor of 0.53 is needed to reconcile the two solutions. This factor is highly dependent on the width of the compliant zone and for more complex rheological variations the factor cannot be estimated. Consider two limiting cases. First, when the width of the compliant zone is much less than the depth of the top of the fault the relationship between body force and slip will be $\rho = \mu_1 s$. Second, when the width of the compliant zone is much greater than the depth to the top of the fault the relationship between body force and slip will be $\rho = \mu_2 s$. Therefore when this numerical approach is used for simulating complex fault systems in areas of variable rigidity, the unknown in the solution will be the force couple (or seismic moment) rather than the slip rate (or slip).

BM5. Model of displacement from a point load on the surface of an elastic half-space. The analytic solution is derived in Love [1944]. The vertical displacement and displacement difference are calculated at a depth of 4 times the horizontal grid cell spacing (Figure 5). The radial displacement (not shown) fits equally well.

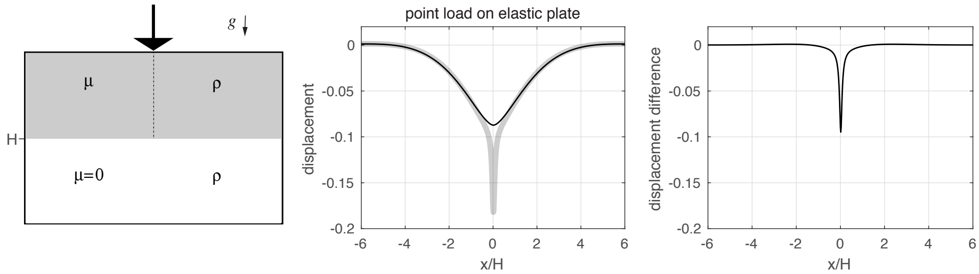

Figure 6: (left) Point load on an elastic plate of thickness H and density ρ overlying a fluid halfspace. (center) The semi-analytic *maxwell* calculation of the surface vertical displacement is compared with the analytical solution for flexure of a thin elastic plate (black line). (right) The solutions agree at a distance of more than one plate thickness H from the load but the numerical solution is more accurate at the smaller distances where the full 3D semi-analytic solution is used.

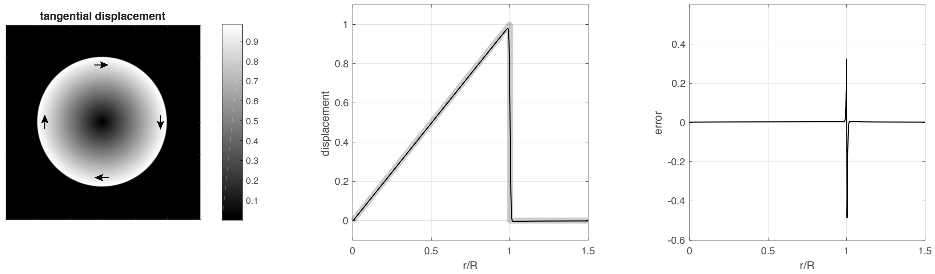

Figure 7: (left) Tangential displacement for a circular strike-slip fault that has uniform slip over the full thickness of the elastic plate. (center) The plate undergoes rigid body rotation so the circumferential displacement increases linearly with distance from the center of the plate. (right) The largest differences between the numerical model and the expected rotation occur above the force couple, which has a finite width so cannot simulate a step.

BM6. Model of a displacement from a point load on an elastic plate of thickness H over a fluid half-space (Figure 6). The half-space has a uniform density of ρ so the restoring force is $-g\rho W$ where g is the acceleration of gravity and W is the vertical displacement. The solution for flexure of a thin elastic plate is used as an analytic approximation (e.g., Banks et al. [1977]). The full semi-analytic solution is derived in Smith and Sandwell [2004]. The differences are greatest where the thin plate approximation fails to simulate the local 3D deformation.

BM7. Model of slip on a circular strike-slip fault in an elastic plate over a fluid half-space (Figure 7). The fault extends through the plate so the circular area of radius R undergoes rigid body rotation, which provides the known solution. The differences are greatest at $r = R$, or the radius distance where the force couple is applied.

BM8. 3D model of a slip on a vertical strike-slip fault in an homogeneous elastic half-space (Figure 8). The analytic solution is provided in Okada [1985] and the semi-analytic solution is provided in Steketee [1958] and implemented using grids of force couples in Smith and Sandwell [2003]. A 4096 × 4096 computational array is used for computation, however only the local faulted region is shown in Figures 8–11.

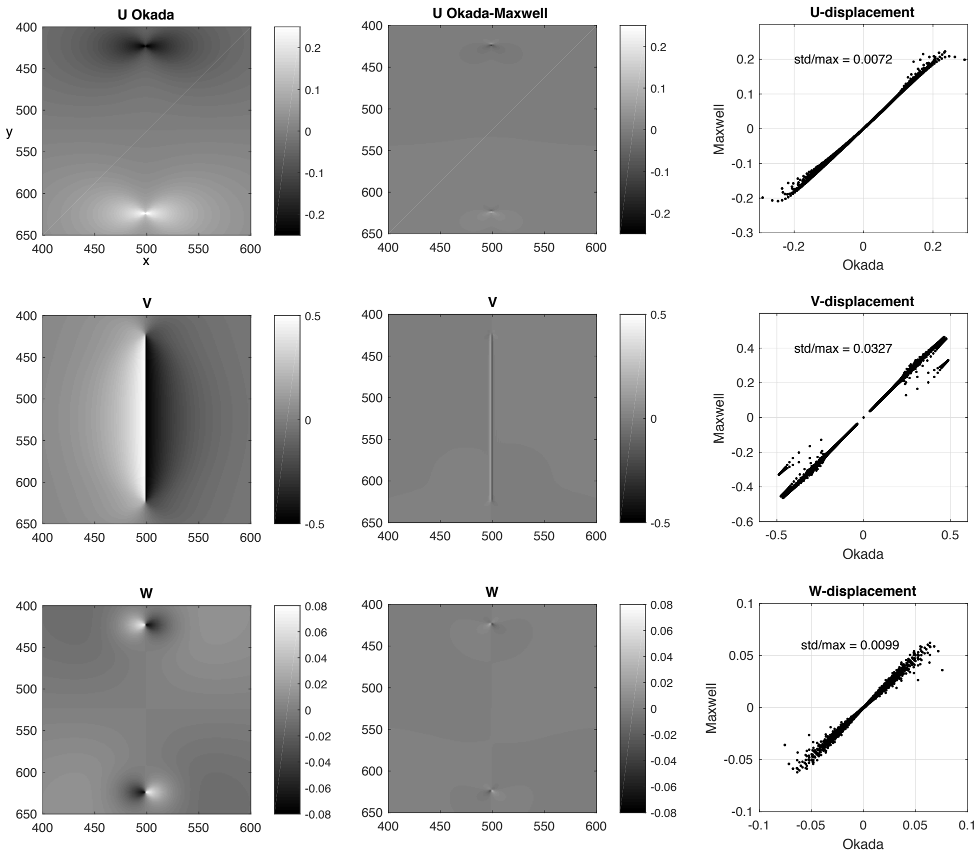

Figure 8: (left) Three components of displacement from slip on a vertical strike-slip fault of length 200 km extending from the surface to a depth of 15 km in an elastic half-space. (center) Differences between the semi-analytic *maxwell* model and analytic Okada model are small away from the fault and larger directly on the fault where the finite size of the force couples does not match the step from the dislocation. (right) Scatter plot comparison of the two models. The standard deviation of the misfit is normalized by the maximum amplitude (std/max). The agreement is better than 1% for the U and W displacements but larger for the V displacement because of the above-fault differences.

BM9. 3D model of slip on a vertical strike-slip fault in an elastic plate over a viscoelastic half-space with the vertical restoring force of gravity (Figure 9). There is no analytic solution for this case so the propagator approach of Fukahata and Matsu'ura Fukahata and Matsu'ura [2006] is compared with the semi-analytic approach of Smith and Sandwell [2004]. Note that this is the total viscoelastic response following the slip event so for the *maxwell* model, the instantaneous elastic solution BM8 was subtracted from the infinite time viscoelastic solution Smith and Sandwell [2004]. Note that the along-strike (V) viscoelastic displacement is in the same direction as the elastic displacement (Figure 8). In contrast, the vertical viscoelastic displacement has an opposite sign and larger amplitude and wavelength than the elastic displacement (i.e., Pollitz et al. [2001]).

BM10. 3D model of slip on a deep vertical strike-slip fault in an elastic plate over a viscoelastic half-space with the vertical restoring force of gravity (Figure 10). This is the same as BM9 but in this case the fault cuts through the entire plate. The fault parallel (V) viscoelastic displacement has the same sign as the elastic displacement. The propagator and *maxwell* models disagree in the vertical where the propagator model has the same sign as the elastic vertical displacement whereas the *maxwell* model has the opposite sign, also consistent with BM9 results. Without a third model for comparison it is impossible to determine which model is more accurate.

4. Discussion: The San Andreas Fault System with Spatially Variable Elasticity

The final case we present here is not a formal benchmark because we have no solution to use for comparison. This case illustrates the effects of spatial variations in rigidity on the surface displacement (or rather, velocity) field. For this case, we constructed a coarse but physically plausible map of spatial variations in rigidity for the SAFS based on a regional heat flow model Thatcher et al. [2017]. Under steady state conditions, the thickness of the elastic plate is proportional to the inverse of the heat flow Turcotte and Schubert [2014]. We crudely simulate plate thickness variations in a constant thickness plate by varying the rigidity to be inversely proportional to heat flow.

The maps in Figure 11 show the main segments of the SAFS used in Tong et al. [2014], projected into a Cartesian coordinate system where the y-axis (positive north) lies along a small circle represented by the best fitting pole-of-deformation (PoD) as derived in Wdowinski et al. [2007]. The algorithm and computer code for performing the PoD projection are more fully described in Appendix B. In our variable rigidity representation, the average rigidity of the area is set to 30 GPa. There are also two areas of higher rigidity of 40 GPa (marked by cyan contours) and two areas of lower rigidity of 20 GPa (marked by magenta contours) that roughly follow heat flow estimates. A 25 km half-wavelength Gaussian low-pass filter was used to smooth the rigidity variations. Using the best-fit slip rates from Tong et al. [2014], we calculated the vector surface velocity with variable rigidity and constant rigidity models. The top row of maps in Figure 11 shows the deformation for the variable rigidity while the lower maps show the variable rigidity with the uniform rigidity models subtracted. The differences highlight the effects of spatial variations in rigidity.

The main difference occurs surrounding the southernmost segments of the SAFS where the variable rigidity model produces higher fault-parallel (V) velocities, especially near the Imperial fault where the increase is ~6 mm/yr on each side of the fault. These velocity increases are centered in an area of lower rigidity. The higher velocities diminish at the northern end of the

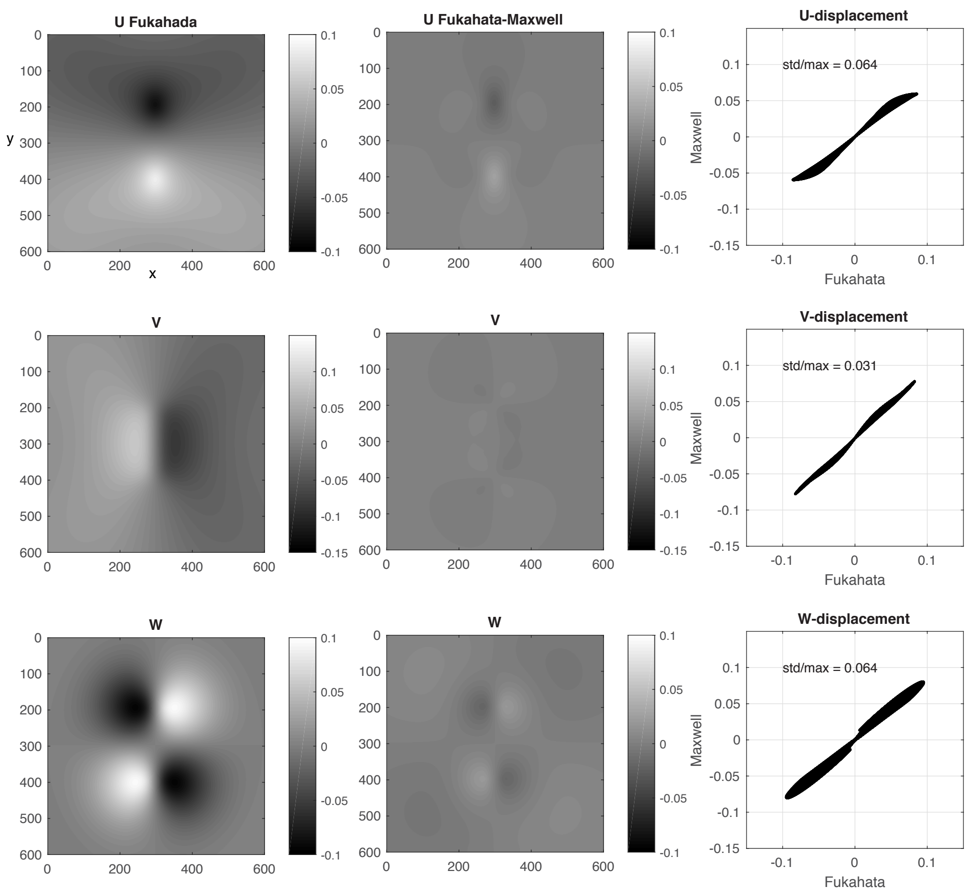

Figure 9: (left) Three components of displacement from slip on a vertical strike-slip fault of length 200 km extending from the surface to a depth of 15 km in an 30 km thick elastic plate over a fluid half-space. The initial elastic response has been removed so this represents the viscoelastic response at infinite time. Truth results are based on a numerical model by Fukahata and Matsu'ura Fukahata and Matsu'ura [2006]. (center) Differences between the semi-analytic *maxwell* model and numerical Fukahata models. (right) Scatter plot comparisons of the two models. The standard deviation of the misfit is normalized by the maximum ampitude (std/max). The agreement is better than 7% for all three components.

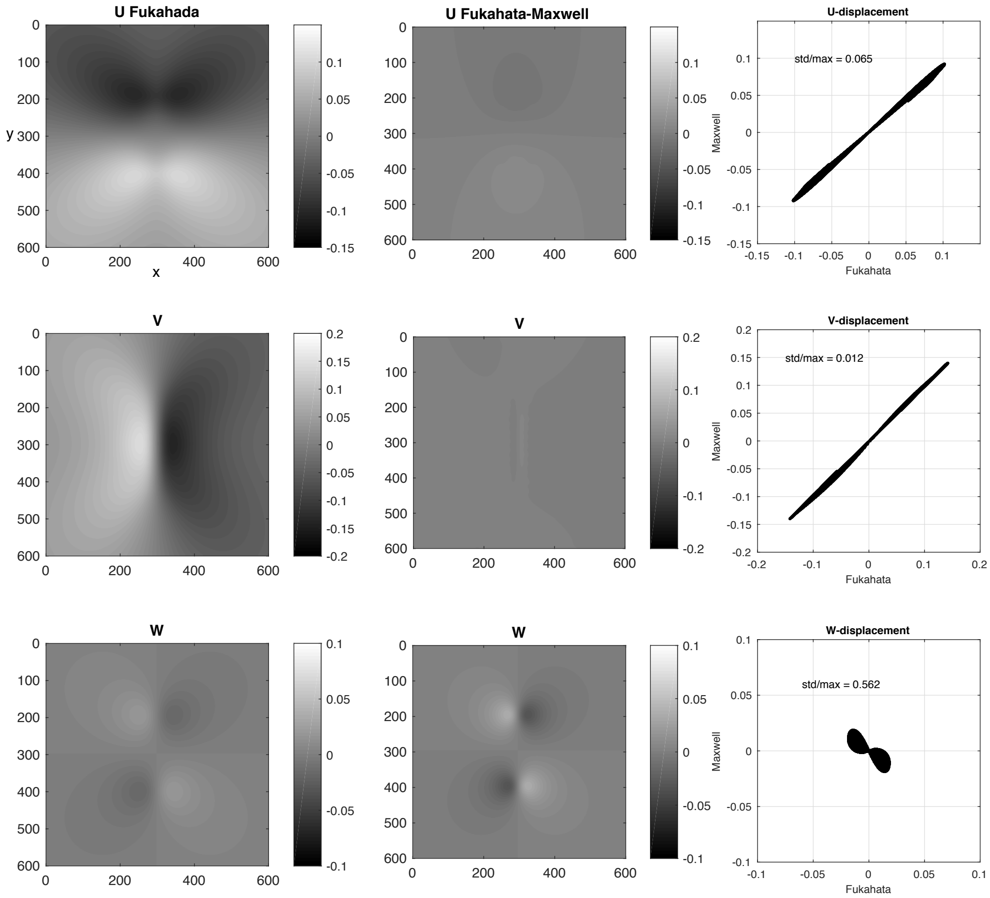

Figure 10: (left) Three components of displacement from slip on a vertical strike-slip fault of length 200 km extending from the surface to a depth of 30 km in a 30 km thick elastic plate over a fluid half-space. The initial elastic response has been removed so this represents the viscoelastic response at infinite time. Truth results are based on a numerical model by Fukahata and Matsu'ura Fukahata and Matsu'ura [2006]. (center) Differences between the *maxwell* and Fukahata models. (right) Scatter plot comparisons of the two models. The standard deviation of the misfit is normalized by the maximum ampitude (std/max). The agreement is better than 7% for the horizontal components but the vertical component has a sign difference. This is an especially challenging case because the fault has unit slip from the surface to the base of the elastic layer.

low rigidity zone where there is a corresponding decrease in the fault perpendicular (U) velocity. It is interesting to note that the velocity differences are small in all areas far from the fault.

This velocity increase in a region of lower rigidity is to be expected based on the results for BM4. In this benchmark, the force couple was not changed when the low-rigidity compliant zone was introduced, causing an amplification in the deformation profile across the fault. We arbitrarily reduced the force couple by a factor of 0.53 to achieve a good match. Similarly, the results shown in Figure 11 would not match the GPS and InSAR data used by Tong et al. [2014] to constrain the slip rates. Therefore, after introducing lateral variations in rigidity, one must re-do a slip-rate inversion. The new unknowns will be moment rate rather than slip rate as in the typical geodetic inversions. While geologists are more interested in slip rate for comparison with geological rates, moment rate is the most important parameter for earthquake hazard analysis Field et al. [2014]. One immediate implication for the Imperial fault is that if the region has relatively low rigidity, then the moment accumulation rate must be smaller than has been estimated using a uniform rigidity model. This implies a lower seismic hazard in the region. The main objective of this model is to use lithospheric rheology models Thatcher et al. [2017] to improve seismic hazard models.

5. Conclusions

We have added lateral variations in shear modulus to an existing computer code (*maxwell*) that is used for simulating time-dependent deformation and stress in complex transform fault systems. The code was tested using 8 analytic solutions for 2D and 3D cases. The more complex 3D viscoelastic response was validated through a comparison with published results based on a propagator matrix approach. Two of the benchmarks included sharp step-like variations in shear modulus that were accurately modeled using the iterative spectral approach, although 20 iterations were needed for convergence. The full San Andreas Fault System model needed only 4 iterations for convergence because the variations in rigidity were smooth (~25 km) relative to the grid spacing of 1 km. The model uses force couples to simulate the faults that drive the deformation. As expected, we find that a decrease in shear modulus in a region surrounding a force couple results in an increase in deformation. Therefore geodetic inversions using this approach will need to solve for moment rate rather than slip rate. The *maxwell* computer code, as well as the coordinate transformation code (*trans_pole*) and scripts needed to reproduce all the examples (Figures 1–11), are available on GitHub.

Appendix A. MAXWELL: Description of the Software Installation, Testing, and Running Benchmarks

This appendix describes the *maxwell* software distribution. The code is available online through GitHub and also as a single tar file. At the upper level there are 5 standard UNIX directories. After unpacking the tar file one should compile and test the code following the instructions provided in `doc/README_compile_test_maxwell`. You will need C and Fortran compilers. Also the reading and writing of grid files uses the GMT library. There are two FORTRAN callable subroutines `lib/readgrd.c` and `lib/writegrd.c` with versions for GMT5 and GMT4. You may need to modify all the makefiles to have the correct paths to the GMT distribution. Also you could replace these routines with your favorite grid file format. The code should be tested using the test examples in `tests/test_maxwell_point`. The tests compare

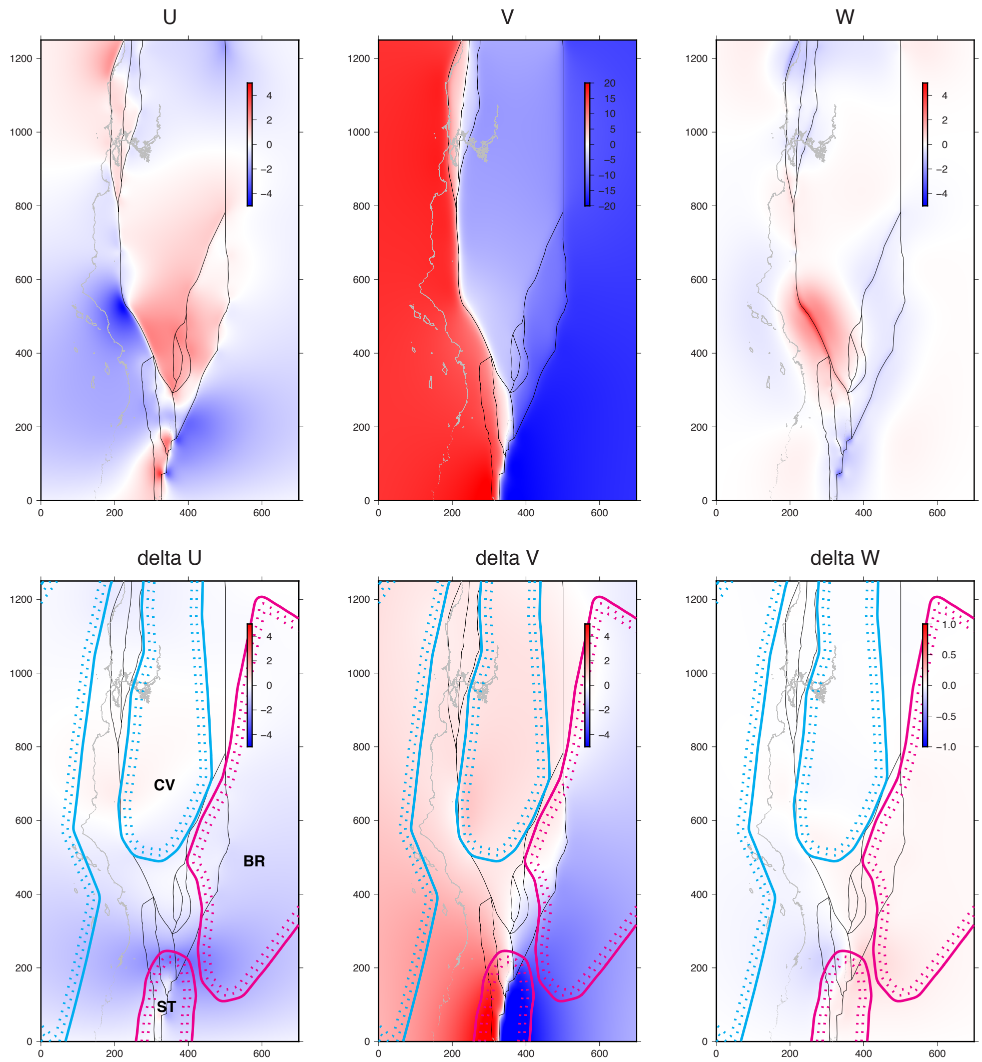

Figure 11: (top) Three components of interseismic surface deformation driven by slip along segments of the SAFS within a 30-km thick elastic plate. Faults are locked from the surface to 10 km depth and slip from 10 to 30 km. (bottom) The shear modulus of the plate varies from a low value of 20 GPa inside the magenta areas (i.e., Salton Trough (ST), Basin and Range (BR)) to a high value of 40 GPa inside the cyan areas (i.e., Central Valley (CV) and ocean lithosphere). All other areas have a medium value of 30 GPa. The three components are the difference between the deformation with a variable rigidity and a constant rigidity. The largest differences occur in the Salton Trough area.

the output with known solutions and report on any differences. After successfully running the test exercise, one can reproduce all the benchmarks provided in this manuscript although Matlab and GMT5 will be needed to construct figures.

```
bin:
maxwell point trans_pole

doc:
JGR_visco1_2004.pdf README_compile_test_maxwell tests.pdf
JGR_visco2_2006.pdf README_src_code_maxwell

include:
halfspace.h layered.h layered_pg.h plate.h

lib:
boussinesq.f coefl.c fourt.f fterm.f makefile readgrd_4.c
writegrd_5.c boussinesql.f coulomb.f fourtd.f fvisco.f makefile_4
readgrd_5.c coefan.f element.f fplate.f libfftfault.a makefile_5
writegrd_4.c

src:
maxwell point test_rw trans_pole

tests:
B1_B4_2D B7_circle B9_B10_Fukahata test_maxwell_point
B5_B6_point B8_Okada B11_SAF
```

Appendix B. TRANS_POLE: Scalar, Vector, and Tensor Data Projection

Our objectives are to project geospatial data from the standard latitude-longitude coordinate system to an approximate Cartesian coordinate system with the *y*-axis parallel to the relative plate motion and the *x*-axis perpendicular to the relative plate motion vector. These transformations are largely provided in Wdowinski [1998]. This coordinate system is defined by the pole of deformation or PoD. The geometry is shown in Figure B.1.
The relevant parameters are:

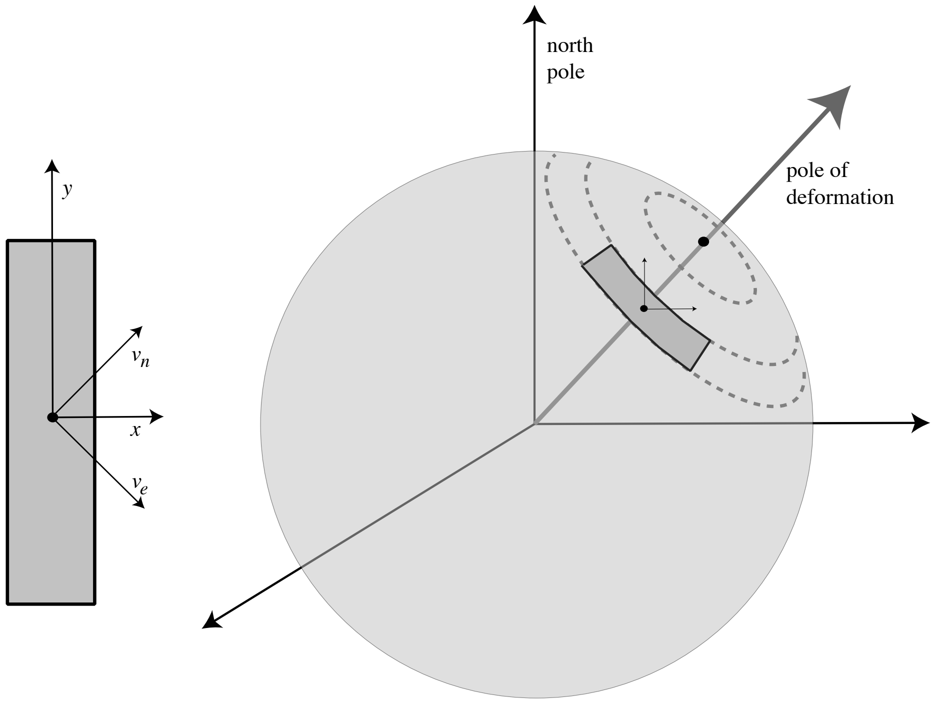

Figure B.1: Schematic diagram showing a small patch (darker gray) containing a ridge/transform plate boundary. The transform faults lie on a small circles about the pole of deformation.

ϕ_p	– longitude of pole
θ_p	– latitude of pole
ϕ	– longitude of point
θ	– latitude of point
ϕ_c	– longitude of center of x-y region
θ_c	– latitude of center of x-y region
x	– distance from center in direction of pole
y	– distance from center along small circle about pole
$s(\phi,\theta)$	– scalar function such as topography or Coulomb stress
$s(x,y)$	– scalar function such as topography or Coulomb stress
$\mathbf{v}(\phi,\theta)$	$= v_e(\phi,\theta)\hat{e} + v_n(\phi,\theta)\hat{n}$ – relative velocity vector
$\mathbf{v}(x,y)$	$= u(x,y)\hat{\imath} + v(x,y)\hat{\jmath}$ – relative velocity vector
$\underline{\mathbf{T}}(\phi,\theta)$	$= \begin{pmatrix} T_{ee} & T_{en} \\ T_{en} & T_{nn} \end{pmatrix}$ – 2D tensor such as stress or velocity uncertainty
$\underline{\mathbf{T}}(x,y)$	$= \begin{pmatrix} T_{xx} & T_{xy} \\ T_{xy} & T_{yy} \end{pmatrix}$ – 2D tensor such as stress or velocity uncertainty

Appendix B.1. Coordinate Mapping

The forward mapping from geographic position (θ,ϕ) to PoD position (θ',ϕ') is performed by first converting the geographic position to a unit vector $\mathbf{r}$, rotating that unit vector into the PoD frame, $\mathbf{r}'$ and finally extracting the new latitude and longitude. The conversion between latitude/longitude and Cartesian coordinate $\mathbf{r} = (r_1, r_2, r_3)$ is given by

$$\begin{aligned} r_1 &= \cos\theta\cos\phi \\ r_2 &= \cos\theta\sin\phi \\ r_3 &= \sin\theta \end{aligned} \tag{B.1}$$

and the inverse transformation is

$$\begin{aligned} \theta &= \sin^{-1}(r_3) = \tan^{-1}\left(\frac{r_3}{\sqrt{r_1^2+r_2^2}}\right) \\ \phi &= \tan^{-1}\left(\frac{r_2}{r_1}\right) \end{aligned} \tag{B.2}$$

Two rotations are needed to transform from the geographic to the PoD coordinate system defined by the rotation pole $\left(\phi_p,\theta_p\right)$.

$$\mathbf{r}' = \mathbf{R_2}\left(\theta_p - \frac{\pi}{2}\right)\mathbf{R_3}\left(-\phi_p\right)\mathbf{r} \tag{B.3}$$

where

$$\mathbf{R_2}(\beta) = \begin{pmatrix} \cos\beta & 0 & \sin\beta \\ 0 & 1 & 0 \\ -\sin\beta & 0 & \cos\beta \end{pmatrix} \tag{B.4}$$

$$\mathbf{R}_3(\gamma) = \begin{pmatrix} \cos\gamma & -\sin\gamma & 0 \\ \sin\gamma & \cos\gamma & 0 \\ 0 & 0 & 1 \end{pmatrix} \tag{B.5}$$

Similarly if one were given the Cartesian coordinate in the PoD frame and wanted to convert back to the geographic frame then the following transformation would be used.

$$\mathbf{r} = \mathbf{R_3}\left(\phi_p\right)\mathbf{R_2}\left(\frac{\pi}{2} - \theta_p\right)\mathbf{r}' \tag{B.6}$$

One final issue is that we want to convert the position in the PoD frame to an SI distance unit relative to an origin. The approach would be to convert the center coordinate of the fault map to the PoD coordinates $(\phi_c, \theta_c) \rightarrow (\phi'_c, \theta'_c)$. We can select any point for this, but a point somewhere in the center of the model space is best. The x-y coordinates are

$$\begin{aligned} x &= R_e\left(\theta'_c - \theta'\right) \\ y &= R_e \cos\theta'_c \left(\phi'_c - \phi'\right). \end{aligned} \tag{B.7}$$

Appendix B.2. Velocity Vector Rotation

When transforming a velocity vector field, one must rotate the east and north vector into the PoD frame. Again, a rotation matrix will be used for both the forward the inverse transformations.

$$\begin{aligned} \begin{pmatrix} v'_e \\ v'_n \end{pmatrix} &= \begin{pmatrix} \cos\gamma & -\sin\gamma \\ \sin\gamma & \cos\gamma \end{pmatrix}\begin{pmatrix} v_e \\ v_n \end{pmatrix} \\ \begin{pmatrix} v_e \\ v_n \end{pmatrix} &= \begin{pmatrix} \cos\gamma & \sin\gamma \\ -\sin\gamma & \cos\gamma \end{pmatrix}\begin{pmatrix} v'_e \\ v'_n \end{pmatrix} \end{aligned} \tag{B.8}$$

The problem is to find the angle of rotation γ between the old and new frames for each point $\mathbf{q}$. Consider the three relevant unit vectors for this problem.

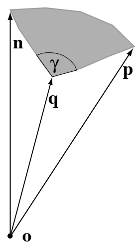

n – unit vector to north pole
p – pole of deformation unit vector
q – position unit vector for a point on Earth

The cross product of **n** and **q** is a unit vector that is perpendicular to the plane formed by **n**-**o**-**q**. The cross product of **q** and **p** is perpendicular to the plane formed by **q**-**o**-**p**. The angle between these two unit vectors is the angle of rotation γ. The formula for sin of this angle is $\sin\gamma = |(\mathbf{n}\times\mathbf{q})\times(\mathbf{q}\times\mathbf{p})|$ and for the cosine of this angle is $\cos\gamma = (\mathbf{n}\times\mathbf{q})\bullet(\mathbf{q}\times\mathbf{p})$. Combining these equations provides the full range of angles

$$\tan\gamma = \frac{\sin\gamma}{\cos\gamma} \tag{B.9}$$

Appendix B.3. Stress Tensor Rotation

As in the case of transforming the velocity vector, we will rotate the stress tensor about the vertical axis by an angle γ. Given the stress tensor

$$\underline{\mathbf{T}} = \begin{pmatrix} T_{xx} & T_{xy} \\ T_{xy} & T_{yy} \end{pmatrix} \tag{B.10}$$

we would like to rotate it into a new primed system $\mathbf{T}'$ as given by the following equation

$$\mathbf{T}' = \mathbf{R}\mathbf{T}\mathbf{R}^T \tag{B.11}$$

where the rotation matrix is given by

$$\mathbf{R} = \begin{pmatrix} \cos\gamma & -\sin\gamma \\ \sin\gamma & \cos\gamma \end{pmatrix} \tag{B.12}$$

In practice these transformations are done with the C-program *trans_pole.c*. Below is the usage statement of *trans_pole*. Table B.1 describes input and output organization.

trans_pole dir dim lonp latp lonc latc < indata > outdata

dir	(1) forward (−1) inverse (lon, lat) (−2) inverse (y, x)
dim	(0) lon, lat – coastline file or fault segment file (out of bounds lon or lat signifies a line gap) (1) lon, lat, scalar – point values of topography or some other scalar (2) lon, lat, ve, vn, se, sn, ren (3) lon, lat, T_{xx}, T_{xy}, T_{yy}
lonp	longitude of pole
latp	latitude of pole
lonc	longitude of center of Cartesian space
latc	latitude of center of Cartesian space
indata	ascii file of 2 (dim = 0), 3 (dim = 1), or 7 (dim = 2) columns to be transformed
outdata	ascii output file with additional columns added

Type	**dim**	**1**	**2**	**3**	**4**	**5**	**6**	**7**	**8**	**9**	**10**	**11**	**12**	**13**	**14**	**15**	**16**
line	0	lon x	lat y	0	lon′	lat′	x	y									
scalar	1	lon x	lat y	t	lon′	lat′	x	y									
velocity	2	lon x	lat y	ve	vn	se	sn	r	lon′	lat′	ve′ vy	vn′ vx	se′	sn′	r′	x	y
tensor	3	lon x	lat y	T_{xx}	T_{xy}	T_{yy}	lon’	lat’	T'_{xx}	T'_{xy}	T'_{yy}	x	y				

Shaded boxes are required for input. x and y are input fields for inverse transformation.

Table B.1: Input and output data columns.

Acknowledgements

We would like to thank Yukitoshi Fukahata for providing his numerical results for benchmarks 9 and 10. This work was partially funded by the NASA Earth Surface and Interior Program (NNX16AK93G), NSF (EAR1614875 and EAR1147427). This research was also supported by the Southern California Earthquake Center (Contribution No. 8007). SCEC is funded by NSF Cooperative Agreement EAR-1033462 and USGS Cooperative Agreement G12AC20038.

References

Banks, R., Parker, R., and Huestis, S. (1977). Isostatic compensation on a continental scale: local versus regional mechanisms. *Geophysical Journal International*, 51(2):431–452.

Barbot, S. and Fialko, Y. (2010). A unified continuum representation of post-seismic relaxation mechanisms: semi-analytic models of afterslip, poroelastic rebound and viscoelastic flow. *Geophysical Journal International*, 182(3):1124–1140.

Barbot, S., Fialko, Y., and Sandwell, D. (2008). Effect of a compliant fault zone on the inferred earthquake slip distribution. *Journal of Geophysical Research: Solid Earth*, 113(B6).

Barbot, S., Fialko, Y., and Sandwell, D. (2009). Three-dimensional models of elastostatic deformation in heterogeneous media, with applications to the Eastern California Shear Zone. *Geophysical Journal International*, 179(1):500–520.

Bürgmann, R., Ergintav, S., Segall, P., Hearn, E., McClusky, S., Reilinger, R., With, H., and Zschau, J. (2002). Time-dependent distributed afterslip on and deep below the Izmit earthquake rupture. *Bulletin of the Seismological Society of America*, 92(1):126–137.

Burridge, R. and Knopoff, L. (1964). Body force equivalents for seismic dislocations. *Bulletin of the Seismological Society of America*, 54(6A):1875–1888.

Chuang, R. and Johnson, K. (2011). Reconciling geologic and geodetic model fault slip-rate discrepancies in Southern California: Consideration of nonsteady mantle flow and lower crustal fault creep. *Geology*, 39(7):627–630.

Field, E., Arrowsmith, R., Biasi, G., Bird, P., Dawson, T., Felzer, K., Jackson, D., Johnson, K., Jordan, T., Madden, C., and Michael, A. (2014). Uniform California earthquake rupture forecast, version 3 (UCERF3)–the time-independent model. *Bulletin of the Seismological Society of America*, 104(3):1122–1180.

Fukahata, Y. and Matsu'ura, M. (2006). Quasi-static internal deformation due to a dislocation source in a multilayered elastic/viscoelastic half-space and an equivalence theorem. *Geophysical Journal International*, 166(1):418–434.

Garcia, E., Sandwell, D., and Luttrell, K. (2014). An iterative spectral solution method for thin elastic plate flexure with variable rigidity. *Geophysical Journal International*, 200(2):1012–1028.

Howell, S., Smith-Konter, B., Frazer, N., Tong, X., and Sandwell, D. (2016). The vertical fingerprint of earthquake cycle loading in southern California. *Nature Geoscience*, 9(8):611–614.

Love, A. (1944). *A Treatise on the Mathematical Theory of Elasticity*. Cambridge University Press.

Nur, A. and Mavko, G. (1974). Postseismic viscoelastic rebound. *Science*, 183(4121):204–206.

Okada, Y. (1985). Surface deformation due to shear and tensile faults in a half-space. *Bulletin of the seismological society of America*, 75(4):1135–1154.

Pollitz, F. (1997). Gravitational viscoelastic postseismic relaxation on a layered spherical Earth. *Journal of Geophysical Research: Solid Earth*, 102(B8):17921–17941.

Pollitz, F., Wicks, C., and Thatcher, W. (2001). Mantle flow beneath a continental strike-slip fault: Postseismic deformation after the 1999 Hector Mine earthquake. *Science*, 293(5536):1814–1818.

Rundle, J. (1981). Vertical displacements from a rectangular fault in layered elastic-gravitational media. *Journal of Physics of the Earth*, 29(3):173–186.

Rundle, J. and Jackson, D. (1977). A three-dimensional viscoelastic model of a strike slip fault. *Geophysical Journal International*, 49(3):575–591.

Rybicki, K. (1971). The elastic residual field of a very long strike-slip fault in the presence of a discontinuity. *Bulletin of the Seismological Society of America*, 61(1):79–92.

Sandwell, D. (1984). Thermomechanical evolution of oceanic fracture zones. *Journal of Geophysical Research: Solid Earth*, 89(B13):11401–11413.

Segall, P. (2010). *Earthquake and volcano deformation*. Princeton University Press.

Simons, M., Fialko, Y., and Rivera, L. (2002). Coseismic deformation from the 1999 Mw 7.1 Hector Mine, California, earthquake as inferred from InSAR and GPS observations. *Bulletin of the Seismological Society of America*, 92(4):1390–1402.

Smith, B. and Sandwell, D. (2003). Coulomb stress accumulation along the san andreas fault system. *Journal of Geophysical Research: Solid Earth*, 108(B6).

Smith, B. and Sandwell, D. (2004). A three-dimensional semianalytic viscoelastic model for time-dependent analyses of the earthquake cycle. *Journal of Geophysical Research: Solid Earth*, 109(B12).

Smith, B. R. and Sandwell, D. T. (2006). A model of the earthquake cycle along the san andreas fault system for the past 1000 years. *Journal of Geophysical Research: Solid Earth*, 111(B1).

Smith-Konter, B. and Sandwell, D. (2009). Stress evolution of the san andreas fault system: Recurrence interval versus locking depth. *Geophysical Research Letters*, 36(13).

Steketee, J. (1958). On Volterra's dislocations in a semi-infinite elastic medium. *Canadian Journal of Physics*, 36(2):192–205.

Takeuchi, C. and Fialko, Y. (2013). On the effects of thermally weakened ductile shear zones on postseismic deformation. *Journal of Geophysical Research: Solid Earth*, 118(12):6295–6310.

Thatcher, W. (1983). Nonlinear strain buildup and the earthquake cycle on the San Andreas fault. *Journal of Geophysical Research: Solid Earth*, 88(B7):5893–5902.

Thatcher, W., Chapman, D., and Allam, A. (2017). Refining Southern California geotherms using seismologic, geologic, and petrologic constraints. In *Annual Meeting of the Southern California Earthquake Center*, page poster 224. August 15., 2017.

Tong, X., Smith-Konter, B., and Sandwell, D. (2014). Is there a discrepancy between geological and geodetic slip rates along the San Andreas Fault system? *Journal of Geophysical Research: Solid Earth*, 119(3):2518–2538.

Turcotte, D. and Schubert, G. (2014). *Geodynamics*. Cambridge University Press.

Wdowinski, S. (1998). A theory of intraplate tectonics. *Journal of Geophysical Research: Solid Earth*, 103(B2):5037–5059.

Wdowinski, S., Smith-Konter, B., and Sandwell, D. (2007). Diffuse interseismic deformation across the Pacific-North America plate boundary. *Geology*, 35(4):311–314.

Weertman, J. (1964). Continuum distribution of dislocations on faults with finite friction. *Bulletin of the Seismological Society of America*, 54(4):1035–1058.